

Detection of X-Ray Doses with Color-Changing Hackmanites: Mechanism and Application

Sami Vuori, Pauline Colinet, Isabella Norrbo, Ralph Steininger, Timo Saarinen, Heikki Palonen, Petriina Paturi, Lucas C. V. Rodrigues, Jörg Göttlicher, Tangui Le Bahers, and Mika Lastusaari*

Hackmanites, a variety of sodalite with the general formula $\text{Na}_8\text{Al}_6\text{Si}_6\text{O}_{24}(\text{Cl},\text{S})_2$, are a family of nature-based smart materials having the ability for reversible photochromism upon UV or X-ray exposure. Being non-toxic, cheap, and durable, hackmanite would be an optimal material for the visual detection of the presence of X-rays in simple portable systems. However, its X-ray-induced coloring abilities are so far known only qualitatively. In this work, a combination of experimental and computational methods is used to reveal the mechanism of X-ray-induced color changing in these materials. Finally, their use is demonstrated both in color intensity-based X-ray dosimetry and photochromic X-ray imaging.

(i.e., F-centers), which are trapped electrons in defect energy levels in the bandgap. With ultraviolet (UV) radiation exposure, the anionic polysulfide species' (e.g., S_2^{2-}) electrons are excited to nearby chloride vacancies where they are trapped. These F-centers are metastable, since visible light and heat can release the electrons back to the sulfur species thus reverting the material to its original color.^[6,8,9] Tenebrescence is also found naturally in minerals, namely tugtupite ($\text{Na}_4\text{AlBeSi}_4\text{O}_{12}\text{Cl}$) and scapolite ($[\text{Na},\text{Ca}]_4\text{Al}_3\text{Si}_9\text{O}_{24}\text{Cl}$), which are used as gems. The phenomenon has been harnessed commercially in the man-

ufacture of lenses, clothing, filters, and smart coatings^[10] and its high potential for easy-to-use personal UV detection has recently been reported by some of us.^[8]

As is the case with detecting UV doses with simple color change, a similar smart visual detection material for X-rays could prove highly usable in warning people of elevated doses in many fields of use. In recent literature, the research on X-ray-induced photochromism for personal X-ray visualization

1. Introduction

Hackmanite ($\text{Na}_8\text{Al}_6\text{Si}_6\text{O}_{24}(\text{Cl},\text{S})_2$) is a naturally occurring variety of the mineral sodalite found in, e.g., Afghanistan, Greenland, Pakistan, USA, and Canada.^[1,2] It exhibits interesting optical properties such as photoluminescence, afterglow, and reversible photochromism, also called tenebrescence.^[3–7] The mechanism is based on the formation of color centers

S. Vuori, Dr. I. Norrbo, Dr. M. Lastusaari
Department of Chemistry
University of Turku
Turku FI-20014, Finland
E-mail: miklas@utu.fi

S. Vuori
Doctoral Programme in Physical and Chemical Sciences
University of Turku Graduate School (UTUGS)
Turku FI-20014, Finland


P. Colinet, Prof. T. Le Bahers
Laboratoire de Chimie (UMR 5182)
Univ Lyon
ENS de Lyon
CNRS
Université Lyon 1
Lyon F-69364, France

Dr. R. Steininger, Dr. J. Göttlicher
Karlsruhe Institute of Technology
DE-76131 Karlsruhe, Germany

Prof. T. Saarinen
Department of Geography and Geology
University of Turku
Turku FI-20014, Finland

Dr. H. Palonen, Prof. P. Paturi
Wihuri Physical Laboratory
Department of Physics and Astronomy
University of Turku
Turku FI-20014, Finland

Prof. L. C. V. Rodrigues
Department of Fundamental Chemistry
Institute of Chemistry
University of São Paulo
São Paulo, SP 05508-000, Brazil

 The ORCID identification number(s) for the author(s) of this article can be found under <https://doi.org/10.1002/adom.202100762>.

© 2021 The Authors. Advanced Optical Materials published by Wiley-VCH GmbH. This is an open access article under the terms of the Creative Commons Attribution License, which permits use, distribution and reproduction in any medium, provided the original work is properly cited.

DOI: 10.1002/adom.202100762

is concentrated on metal–organic systems.^[11–15] On the other hand, hackmanite's ability to color upon X-ray exposure has been known at least from the 1950s,^[6] but its suitability for X-ray detection has not been studied previously. Neither are the mechanisms by which the color is created and bleached known. Thus, only qualitative information exists for this family of smart materials that would have also the advantage of being cheap, durable, and nontoxic.^[8]

The first reports on the X-ray-induced coloration of minerals date back to the late 19th and early 20th centuries,^[6] but during the latter half of the 20th century it was reported broadly for various inorganic materials. It was defined by Doelter as oxidation and reduction changes of metallic oxides: his samples consisted of spodumene ($\text{LiAl}(\text{SiO}_3)_2$), topaz ($\text{Al}_2\text{SiO}_4(\text{F},\text{OH})_2$) and quartz (SiO_2).^[16] However, a further definition was given by Stuhlman and Daniel who concluded that the mechanism originates from the trace KMnO_4 's oxidative property on a silicon compound.^[17] They exposed kunzite ($\text{Li}(\text{SiO}_3)_2$) samples to unfiltered 50 kV, 20 mA X-rays for 4 h and found out that the original pale lilac color changes to deep blue-green through intermediate green shades. In 1947, after the development of an intense source of X-rays (50 kV, 50 mA, intensity several hundred times higher than previously), Pough and Rogers conducted a large experiment using 49 samples of different local variations of spodumene ($\text{LiAlSi}_2\text{O}_6$), beryl ($\text{Be}_3\text{Al}_2\text{Si}_6\text{O}_{18}$), corundum (Al_2O_3), tourmaline (complex silicate), quartz (SiO_2), topaz ($\text{Al}_2\text{SiO}_4 \cdot (\text{F},\text{OH})_2$), diamond (C), spinel (MgAl_2O_4), phenakite (Be_2SiO_4), apatite ($\text{Ca}_5(\text{F},\text{Cl})(\text{PO}_4)_3$), fluorite (CaF_2), opal ($\text{SiO}_2 \cdot n\text{H}_2\text{O}$), scapolite (complex silicate), brazilianite ($\text{Na}_2\text{Al}_6\text{P}_4\text{O}_{14} \cdot 4\text{H}_2\text{O}$), simpsonite ($\text{Al}_{10}\text{Ta}_6\text{O}_{20}$), diopside (H_2CuSiO_4), hackmanite ($\text{Na}_8\text{Al}_6\text{Si}_6\text{O}_{24}(\text{Cl},\text{S})_2$), cancrinite ($(\text{Na}, \text{Ca})_8\text{Al}_6\text{Si}_6\text{O}_{24}(\text{CO}_3, \text{SO}_4)_2 \cdot 2\text{H}_2\text{O}$), lapis lazuli (complex Na aluminosilicate containing lazurite), zircon (ZrSiO_4), chrysoberyl (BeAl_2O_4), and oligoclase ($(\text{Na}, \text{Ca})(\text{Si}, \text{Al})_4\text{O}_8$). Although coloration was observed, the mechanism was not discussed. The experiment's motivation was more on the new X-ray machine's testing and finding new antifraud properties for commercial gems.^[18] In 1953, Claffy reported that the tenebrescence of hiddenite ($\text{LiAl}(\text{SiO}_3)_2$) and spodumene ($\text{LiAl}(\text{SiO}_3)_2$) obtained after 3 h in the X-ray beam is related to the presence of Cr, V, and Mn.^[19] Next year Medved established the groundbreaking tenebrescence theory of hackmanites.^[6] In his article, the mineral was exposed to X-rays, which turned the whitish color purple. According to Medved's theory, this was due to electrons being promoted to the conduction band where they got trapped in the negative ion (Cl^-) vacancies. In addition to Medved, during the same time Kirk published his research on the matter and stated that under UV irradiation the coloration mechanism is due to a Na_2S_x chromophore.^[20,21] With more details added, the early theory of Medved is still well in line with how UV-induced tenebrescence is understood today. It may be that the same theory could apply to X-rays as well, but since the energy of X-rays is very much higher than that of UV radiation, the two mechanisms may also be very different. That is why we set out to investigate the mechanism in detail.

In the present work, we carry out a thorough systematic investigation on the X-ray-induced coloration and subsequent discoloration properties of hackmanites. We employ a set of experimental techniques, including thermotenebrescence, a

method developed by some of us especially for tenebrescence research,^[8] and computational methods to reveal the mechanism of X-ray-induced tenebrescence for the first time. Finally, we show the application of X-ray-induced tenebrescence for passive dosimetry and imaging.

2. Results and Discussion

2.1. Comparison of the UV- and X-Ray-Induced Color Centers

After checking with X-ray powder diffraction that all samples had the correct crystal structure (Figure S1, Supporting Information) and that they showed tenebrescence with UV and X-ray irradiation (Figure 1a), we studied whether there would be differences between the energetics associated with the UV- and X-ray-induced color centers. From previous work, we know that the characteristic properties of the color centers can be defined by a) the threshold energy required to induce coloring, b) the absorption spectrum of the colored material, c) the energy required for the thermal bleaching of the color, d) the energy required for the optical bleaching of the color, and e) the spontaneous decay rate of the color at room temperature. Since we are comparing already-generated color centers, we concentrate on discussing points (b–e) below.

Reflectance spectra shown in Figure 1b can be seen to take a very similar shape with both exposure methods. There are some minor differences, but they are probably due to microscopic inhomogeneities caused by the casting process-induced small deviations in the scattering of light from the surface. Thus, the results suggest that the color centers absorb the same wavelengths regardless of the previous exposure radiation type. The normalized color fading curves (Figure 1c) recorded at room temperature under white light show how the color fades rather similarly with either one of the exposure types. There is some variation, but we expect them to be small enough to be due to experimental inaccuracy. The thermotenebrescence curves^[8] (Figure 1d) show a little more variation, but the thermal bleaching threshold energies obtained using the initial rise method^[8,22] indicate only very small differences between UV- and X-ray-induced color (Figures S2 and S3, Supporting Information). Finally, the tenebrescence bleaching spectra (Figure 1e) likewise show a very small difference in the energy required to bleach UV- and X-ray-induced color centers with optical stimulation.

From the comparative data presented above, we can see that the color centers induced by X-rays and UV do not differ, thus it is proposed that the mechanisms of tenebrescence and bleaching occur in the same manner in both exposure methods. That is, an electron leaves from the $(\text{S}_2)^{2-}$ ion to a chloride vacancy (V_{Cl}) creating a $(\text{S}_2)^- - V_{\text{Cl}}^-$ pair.^[8]

2.2. What Happens During the X-Ray Exposure?

2.2.1. Sulfur Species

Similar to UV-induced tenebrescence, X-ray-induced tenebrescence includes the participation of disulfide ions. We set out to

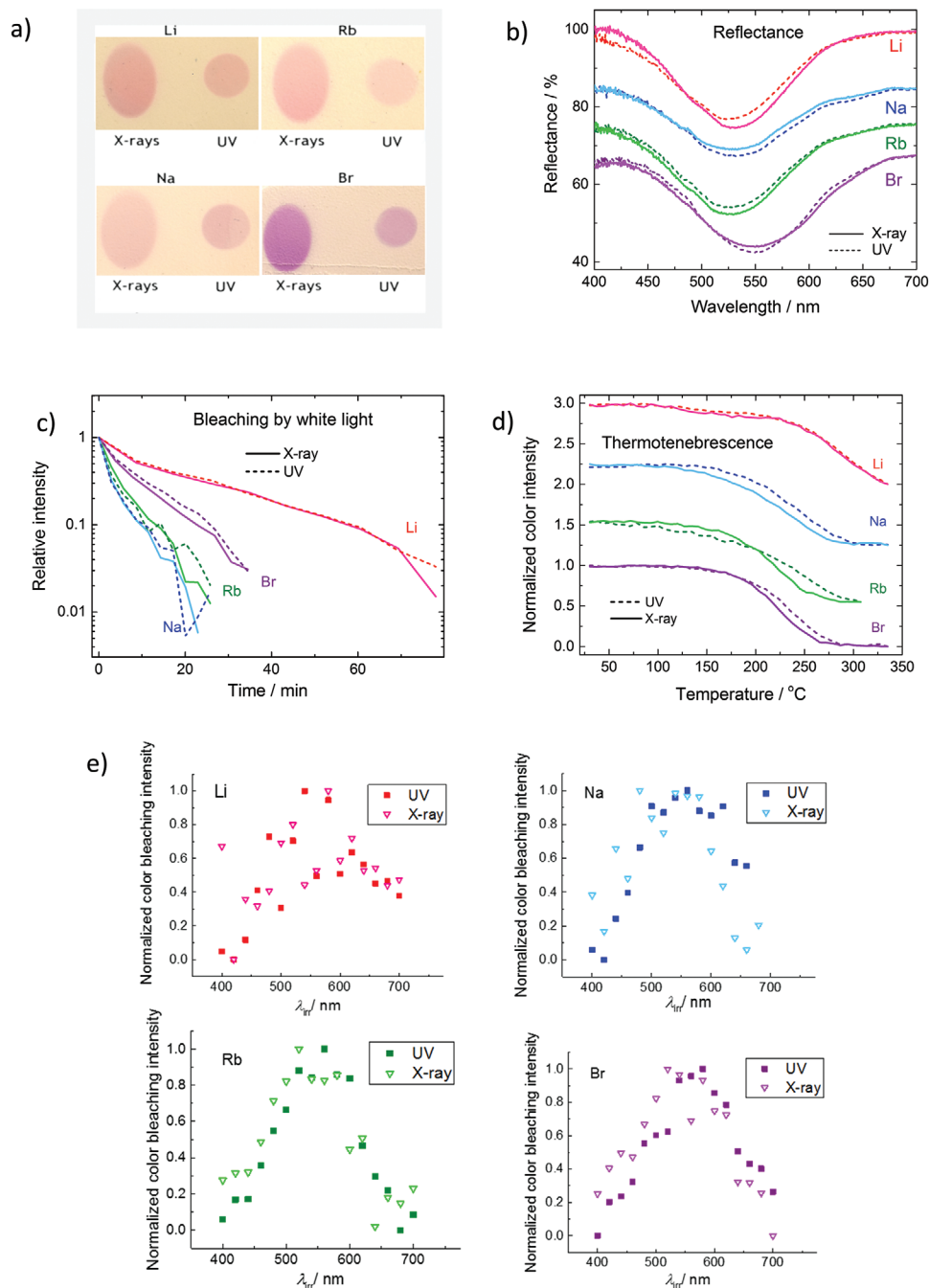


Figure 1. a) Photos of tenebrescence induced with 254 nm UV and 22 keV X-rays. Note that each sample was given an equal UV dose and equal X-ray dose, but the two doses are not the same and thus the color intensities are not comparable between UV and X-rays. The surrounding off-white-colored area is the unexposed part of the tape. b) Reflectance spectra. c) Color fading under white light at room temperature. d) Thermotenebrescence curves. e) Tenebrescence bleaching spectra.

investigate what happens to the sulfur species during the X-ray exposure. That was done by X-ray absorption near-edge structure (XANES) measurements over the sulfur's K edge region.

The most prominent features of the spectra are the pre-edge peak at 2.465 keV, edge peak at 2.471 keV and the sulfate peak at 2.481 keV (Figure 2a). With increasing time in the X-ray beam, the pre-edge peak rises (Figure 2b), the edge peak is gradu-

ally decreasing (Figure 2c) and the sulfate peak is unreactive. These results are in agreement with those reported by some of us earlier.^[23] It is hypothesized that the rising of the pre-edge peak is correlated with the deepening of the tenebrescence, since it saturates with time (Figure S4, Supporting Information) and converges in a similar fashion that has been reported for UV-induced tenebrescence.^[8] Also, the edge peak has been

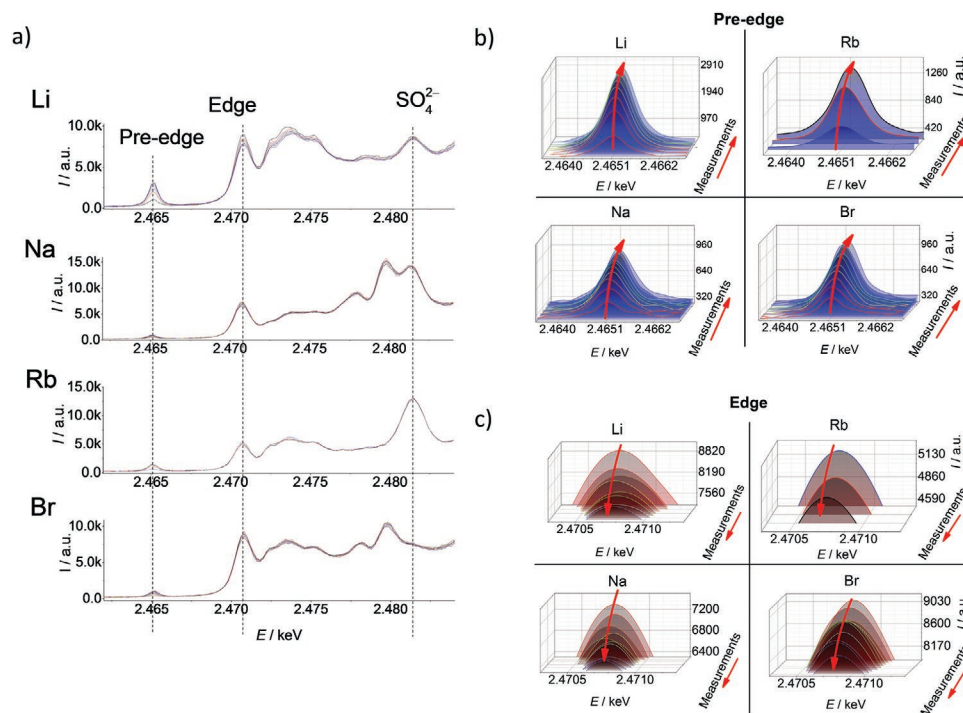


Figure 2. a) XANES spectra. b) The pre-edge peak's evolution with measurements, and c) the edge peak's evolution with measurements.

suggested to be involved in the tenebrescence process. However, no proof of the origin of these peaks or why their intensity changes has been presented before.

To clarify the XANES results we carried out quantum chemical calculations to simulate the XANES spectra of the S_2^{2-} and S_2^- species. These two species are involved in the UV-induced tenebrescence mechanism reported earlier.^[8,9] The calculations were conducted by substituting a Cl anion by S_2^- and S_2^{2-} ions inside a β -cage. The orbital labeling used for XANES transition indexations is presented on the density of states (DOS) of the S_2^{2-} compound inside the hackmanite structure (Figure 3). On this DOS, the S_2^{2-} occupied orbitals (π and π^*) and empty orbital (σ^*) are visible inside the wide bandgap of the hackmanite. The orbitals associated to V_{Cl} can be observed as well. The time-dependent density functional theory simulated K-edge spectra are given in Figure 4a, the experimental one is given in Figure 4b and the virtual orbitals involved in these transitions are given in Figure 4c,d. Obviously, the computed energy range of these transitions is underestimated compared to the experimental one, but it corresponds to a relative error below 0.2% already reported and expected for this method of calculation. Such a small error does not alter the interpretation of the spectra given by the quantum chemical calculations. It is evident from the comparison of the calculated and experimental data that the signal observed at 2.465 keV is due to the $1s \rightarrow \pi^*$ transition of S_2^- . This suggests that each sample is already partly colored before the sulfur K edge energy has been reached. Indeed, this is also seen from photos taken from the samples at energies around the sulfur K edge (Figure S5, Supporting Information). There seems to be no distinct difference between the coloration with different energies, which suggests

that the K-shell electron excitation does not play a significant role in the X-ray-induced V_{Cl} trapping.

If we consider that the experimental energy difference between the sulfur K edges for S^{2-} and S^0 has been reported to be ≈ 1 eV,^[24] we may deduce that the difference between the K edges of S_2^- (corresponding to $\text{S}^{0.5-}$) and S_2^{2-} (S^-) should be of the order of 0.25 eV in experimental XANES spectra. This is smaller than the bandwidth of this transition and thus the signals of the $1s \rightarrow \sigma^*$ transitions of S_2^- and S_2^{2-} will actually overlap completely in the experimental spectrum, i.e., the signal at ≈ 2.471 keV is the sum of these two transitions. With that assumption, we simulated XANES spectra by summing the contribution of S_2^{2-} and S_2^- ion weighted both by the ratio $\text{S}_2^- / \text{S}_2^{2-}$ and by the computed oscillator strengths. The results show that with increasing S_2^- content the peak at 2.465 keV should grow and the peak at 2.471 should diminish (Figure 4e). This agrees well with the experimental results. A further confirmation was obtained by measuring the rise of the 2.465 keV peak for a pre-UV-irradiated sample as the UV treatment resulted in a higher intensity for this peak in the beginning of the X-ray exposure (Figure S7, Supporting Information).

The experimental XANES data show a maximum of 5% variation in the summed intensity of the $1s \rightarrow \pi^*$ and both $1s \rightarrow \sigma^*$ transition signals between the different measurements (Figure S6a, Supporting Information). There isn't any clear trend in the values and thus it seems that the variation is due to experimental errors. This suggests that the total number (sum) of the S_2^{n-} species stays constant during the XANES measurements. Finally, a comparison of the observed intensity ratios of these two peaks with the calculated ones allows us to estimate the $\text{S}_2^- : \text{S}_2^{2-}$ ratio during the XANES measurements.

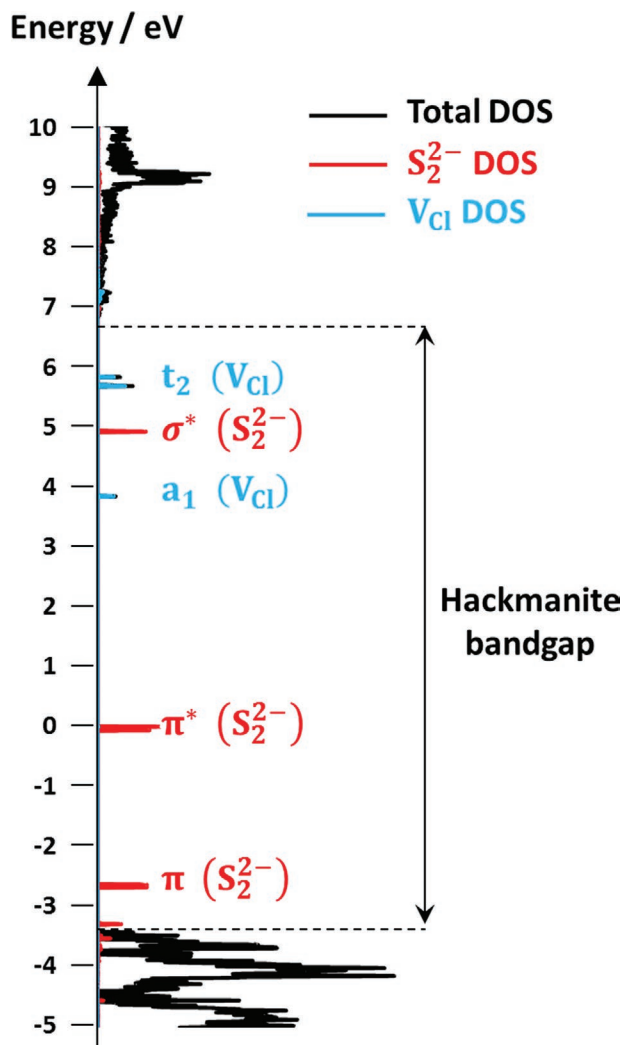


Figure 3. Density of states of the S_2^{2-} substituting a Cl^- and creating a V_{Cl} inside the hackmanite structure.

As an example, for the Li sample, the first measurement indicates $\approx 25\%$ of S_2^- (intensity ratio 0.10; Figure S6b, Supporting Information), which increases to $\approx 95\%$ (intensity ratio 0.56; Figure S6b, Supporting Information) for the sixth measurement (Figure 4f), i.e., with increasing time in the X-ray beam. The simulation results thus confirm that the XANES pre-edge peak at 2.465 keV and the edge peak at 2.471 keV are, indeed, connected with the coloration of the material. More importantly, these results confirm that X-ray-induced tenebrescence includes the same S_2^{2-} to S_2^- oxidation that takes place in the UV-excited tenebrescence mechanism.

2.2.2. Luminescence

During the exposure to X-rays, the sample had a notifiable emission in the UV region peaking at ≈ 400 nm (Figure 5a). This means that hackmanite functions as a scintillator, i.e., as an X-ray-excited optical luminescence (XEOL) material. With

this observation, we know what kind of processes take place during X-ray excitation also in the hackmanites: XEOL is a process where a core hole and an accompanying photoelectron with a high kinetic energy are created through an X-ray photon absorption. The de-excitation can occur through X-ray fluorescence or nonradiatively through the chain reaction of electrons and outer shell holes, finally reaching a ground state where all energy has been consumed, stopping further excitation processes.^[25] In general, this means that the initially created electron-hole pair causes a cascade of an increasing number of electrons as well as a similar cascade of holes. Both lose energy on the way to the bottom of the conduction band (electrons) or top of the valence band (holes). Once they have reached the borders of the bandgap, they will recombine causing bandgap emission. The bandgap emission can then excite other emissions with lower energy. Another characteristic associated with XEOL is that the number of electron-hole pairs created before recombination depends on the initial X-ray photon's energy in such way that higher X-ray energies give more such pairs: for ionic crystals, the number of created electron-hole pairs can be approximated to be $E_{X\text{-ray photon}}/2E_{\text{bandgap}}$.^[25] Ideally, this would lead to the increase of emission intensity with increasing excitation energy, but most scintillator materials follow this ideal behavior only in a limited energy range (typically in the lowest energies).^[26] That is, ideally I/E versus E is horizontally linear, but in practice it is an ascending series since the scintillation luminescence intensity grows with energy. Indeed, we observe such a rise between 5 and 15 keV of synchrotron X-ray excitation for hackmanite, as well (Figure 5b). Additionally, we observed that the XEOL intensity decreases with increasing time in the synchrotron X-ray beam (Figure 5c). A similar decrease was earlier reported for cathodoluminescence in hackmanites.^[27] The emission was then assigned to oxygen vacancies occupied with one electron and thus the decrease of emission intensity was suggested to be due to the filling of the vacancies.^[27] A similar explanation seems plausible also in the present case, because of the high number of thermalizing electrons available to fill oxygen vacancies.

Since the scintillation process initiates bandgap emission (at 77 eV for hackmanite^[3]) and near bandgap emission, we tested how hackmanite can be excited with such energies by recording vacuum-ultraviolet-ultraviolet excited emission spectra (Figure 5d). The results show that with lower excitation energies, hackmanite shows its typical blue/white emission due to $Ti^{3+}\text{-}V_O$ pairs.^[3,5,27] When the excitation energy increases closer to the bandgap energy, the 400 nm band appears together with another band peaking at ≈ 320 nm. The highest excitation energies thus create UV range emission that we expect to be able to color the hackmanite.

To examine the possibility of such auto-excitation, we duplicated the emission intensity observed with 5 keV synchrotron excitation (Figure 5a) by using 302 and 365 nm UV lamps (Figure 5e) placed at such distances where the irradiance corresponds to that observed for hackmanite's XEOL. This means irradiances 1.5×10^{-5} (302 nm) and 1.2×10^{-5} mW cm⁻² (365 nm), i.e., about a factor of 3×10^5 less than the lamps give on the surface of their exit windows. At such low irradiances, the two UV lamps used together could not change hackmanite's color even with 30 min irradiation exposure (Figure 5e).

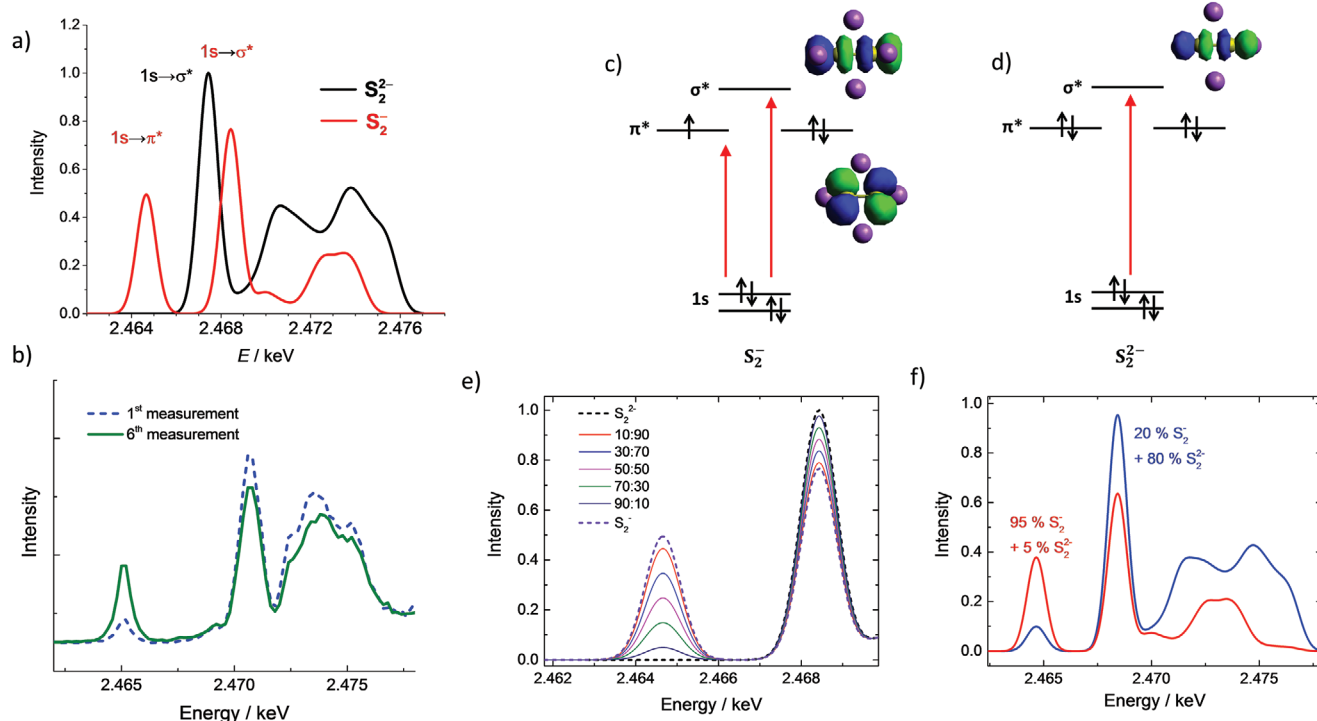


Figure 4. a) Computed sulfur K edge XANES spectrum of S_2^{2-} (black) and S_2^- (red) surrounded by Na_4 tetrahedron and the β -cage embedded in an electrostatic potential (peaks assigned to different transitions). b) Experimental XANES spectra for the Li sample with background subtracted. c, d) Transitions and associated orbitals for S_2^- (c) and S_2^{2-} (d). e) Simulated XANES spectra for bare and different mixtures of S_2^{2-} and S_2^- assuming complete overlap for the $1s \rightarrow \sigma^*$ transition of both species. f) Simulated XANES spectra estimating the S_2^{2-} : S_2^- ratio of the Li sample shown in (b).

This indicates that the hackmanites' own UV emission is not a probable cause of coloration under X-ray irradiation.

2.3. Coloration Efficiency and Effect of X-Ray Energy

For UV-induced tenebrescence in hackmanites, it is known that color saturation is reached in the range of a few minutes, when regular hand-held UV lamps are used for the irradiation and the lamp is placed within a few centimeters from hackmanite.^[8] In this work, we tested the color rise in synchrotron X-ray beam for three different energies (5, 10, 15, and 20 keV). It is evident that neither of the energies results in the saturation of color within 1 h (Figure 6a). Thus, the coloration efficiency of X-rays is clearly weaker than that of UV radiation.

One factor that is highly likely to play a role in the coloration efficiency is hackmanite's ability to absorb X-rays. Since hackmanite is on average composed of rather light elements, its photoelectric absorption is not very high for X-rays and it falls rather quickly with increasing X-ray energy, e.g. from 5 to 20 keV it drops $\approx 99\%$ (Figure 6b). When we take into account this absorption ability and the photon flux of the X-ray beam with different X-ray energies, it is easier to compare the effects more quantitatively: Figure 6c shows that 20 keV produces the faintest coloration, while 5 keV produces the most pronounced effect, and 10 and 15 keV fall between these. When we also take into account the assumption that the number of electron-hole pairs that can induce the coloration is dependent on the X-ray

beam's energy, we end up with descending color yield curves for each material (Figure 6d). This is thus in contrast to what was shown for luminescence above (Figure 5b) and therefore it is unexpected for a process that is very likely to involve a similar mechanism as scintillation. In general, the color yield curves indicate that coloration is best achieved between ≈ 2 and 4 keV. This is the range where the K edges of Si (1.8 keV), Cl (2.8) and K (3.6; impurity in the halide salt starting materials) absorb^[28] and cause corresponding secondary X-ray emission. This suggests that such energy self-down-shifting may be beneficial for the color creation efficiency.

Since it is known that hackmanites also show cathodochromism,^[6,29,30] i.e., tenebrescence induced with electron beam irradiation, we constructed a similar color yield curve with electrons. The results show (Figure 6e) that in the cathode ray beam the color yield behaves as is expected for a scintillation mechanism. Thus, it is not the energy of irradiation as such that makes the coloration yield for X-rays a descending curve, but there must be other reasons.

We suggest that the reason for the coloration not following the scintillation theory completely is because of the thermal bleaching^[8] caused by the intense synchrotron X-ray beam. Synchrotron radiation has been detected to have a major effect on the temperature of the sample: Warren et al. measured a steady-state temperature increase of 70–80 K in a ruby crystal within a time frame of ≈ 40 ms by exposing the sample to 9.2 keV X-rays,^[32] while Kastengren measured a temperature rise of almost 700 K within seconds on an lutetium

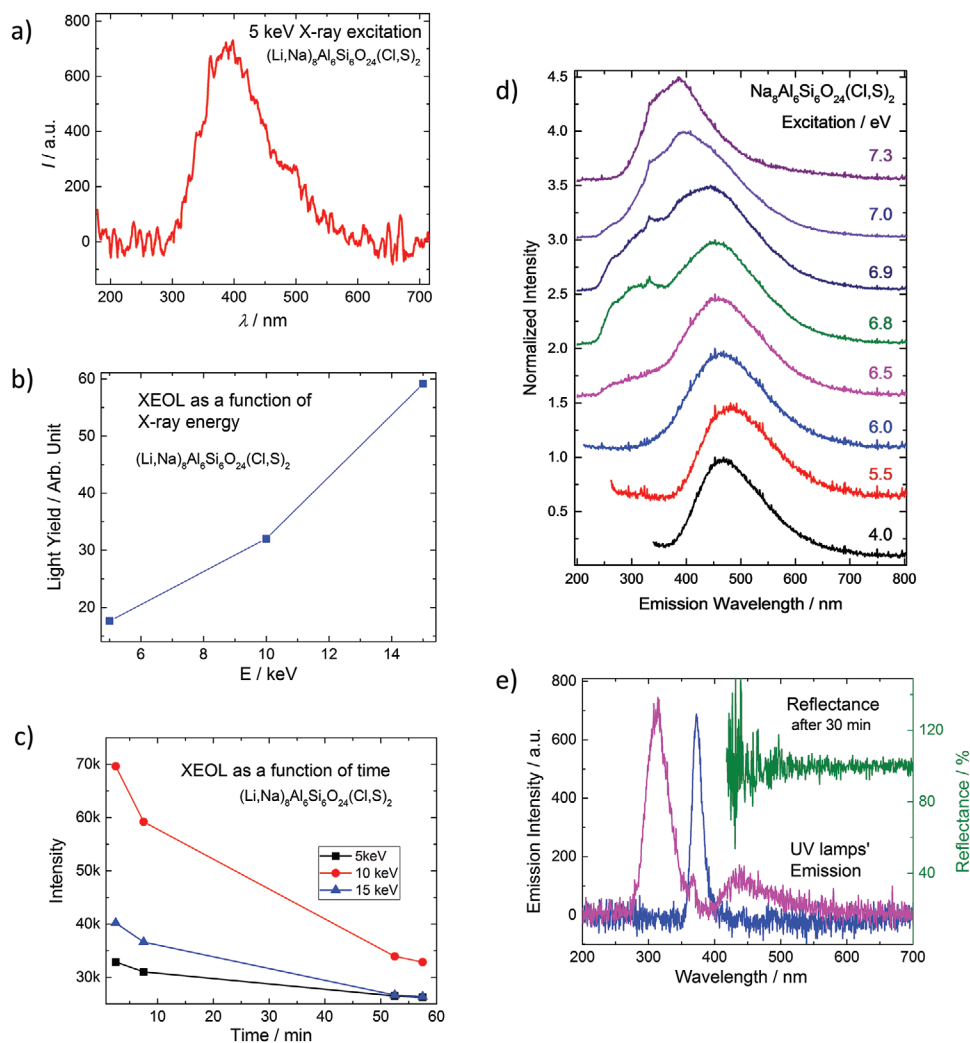


Figure 5. a) The XEOL spectrum of hackmanite with a 5 keV excitation. b) Effect of X-ray energy on the XEOL light yield (= emission intensity/excitation energy). c) Effect of X-ray exposure time on the XEOL emission intensity. d) Emission spectra. e) Spectra of the used UV lamps and reflectance spectrum after 30 min irradiation with the lamps. The data in (b,c) have been corrected for hackmanite's photoelectric absorption intensity and the X-ray beam's dose rate.

oxyorthosilicate scintillator disc with an unfiltered X-ray beam.^[33] Wallander and Wallentin concluded that the temperature rise is a function of synchrotron X-ray beam's flux, with the highest steady-state temperature reaching 700 °C.^[34] In the case of hackmanites, a temperature rise of 70 °C from room temperature would already be enough to induce bleaching as suggested by the thermotenebrescence curves presented above (Figure 1d). Thus it is highly probable that while the X-ray beam induces new color the heat created by it will erase the color partially. When a certain X-ray dose has been reached, the heat and color generation are in equilibrium. Also, as the dose depends on the energy of the radiation,^[35] it can be assumed that if the flux is constant, higher energy translates to increased heat. The interplay between energy, flux, tenebrescence, and heat is thus proposed to explain the unusual results of the coloration process: the heating of the sample gives rise to the fact that higher energies do not induce coloration as much as expected.

In addition to the bleaching effects of heating, one affecting component could be radiation damage: certain persistent luminescence materials (barium/strontium aluminates) have been observed to suffer from radiation damage buildup and decreased XEOL after a prolonged time in the X-ray beam.^[36,37] In general, tenebrescence is a rather similar phenomenon to persistent luminescence since both involve the trapping and gradual release of electrons to/from vacancies. Thus, we could expect similar radiation damage also for tenebrescent materials. A proof of radiation damage, which may also have been caused by excessive heating, can be seen from photos taken of the samples after the synchrotron exposure experiments. Points with the highest doses have lost partially or completely the ability for tenebrescence (Figure 7a,b). Micro X-ray fluorescence (XRF) data indicates that the damage does not change the overall composition (Figure 7c) of the material. Thus, the local temperature in the damaged spot has not been high enough to cause the evaporation of chlorine or sulfur. However, micro

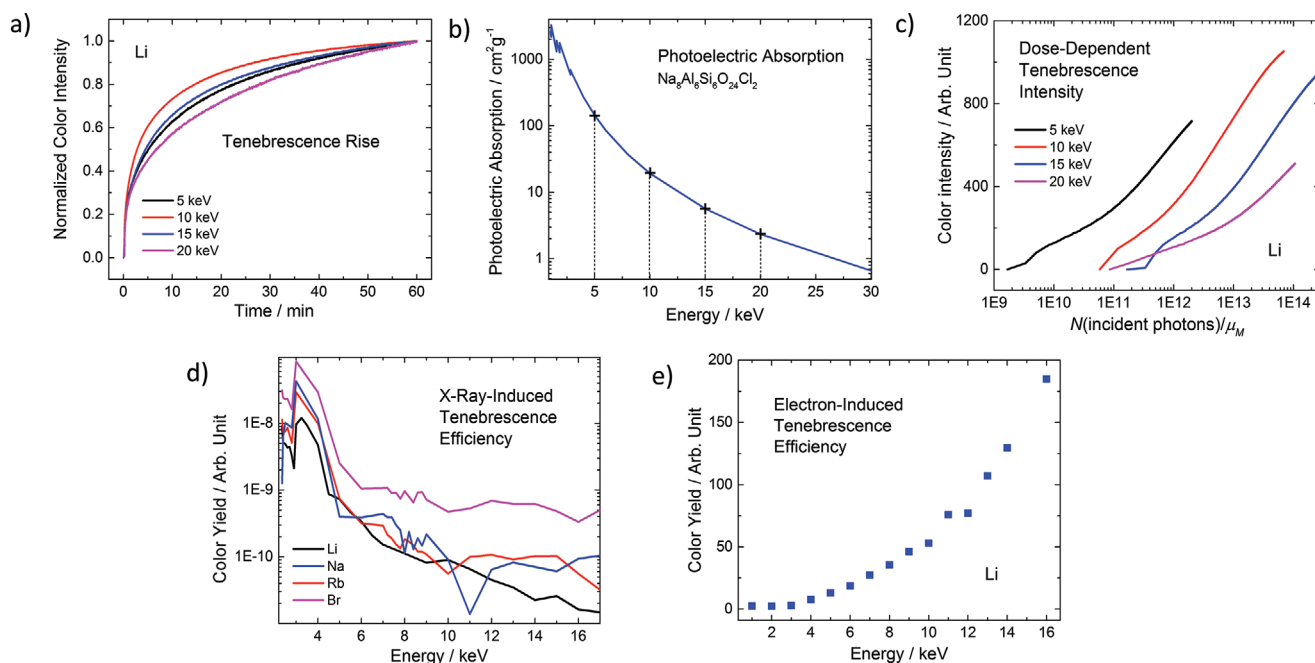


Figure 6. a) Tenebrescence rise curves for the Li material. b) Photoelectric absorption for hackmanite.^[31] c) Color intensity as a function of incident X-ray photons for the Li material. d) Color yield (= color intensity/irradiation energy) in X-ray beam for all materials. e) Color yield in electron beam for the Li material. The data in (d,e) have been corrected for hackmanite's photoelectric absorption intensity and the X-ray beam's dose rate or the electron beam's current.

X-ray diffraction (XRD) indicates one additional reflection at 45.4° due to the damage (Figure 7d). This originates from the (220) reflection of NaCl,^[38] i.e., hackmanite has decomposed partially resulting in the crystallization of NaCl with the (220) faces parallel to the sample surface. A similar growth with (220) preferred orientation has been reported, e.g., for physical vapor-deposited NaCl.^[39] There are no traces of other new phases in the diffraction patterns. Thus, either the other phases are amorphous or NaCl has left the hackmanite structure only partially creating $\text{Na}_{8-x}\text{Al}_6\text{Si}_6\text{O}_{24}\text{Cl}_{2-x}$ still possessing the sodalite structure. Such decomposition definitely decreases the number of intact hackmanite crystallites and thus the overall color intensity that can be obtained from the sample. Also, the decomposition as well as the heating will decrease the XEOL intensity of the material as reported above (Figure 5c).

2.4. Mechanism of X-Ray-Induced Tenebrescence

Above, we have shown that the X-ray-induced color center is similar to that induced by UV radiation, i.e., its absorption peaks in the same wavelength and it can be bleached similarly with visible light and heating. Thus, we can assume that the energy states participating in the mechanism are the same: the ground state $^1[\text{S}_2^{2-}, \text{V}_{\text{Cl}}]$ is excited to $^1[\text{S}_2^-, \text{V}_{\text{Cl}}(a_1)]$ to create the color center with the states $^3[\text{S}_2^-, \text{V}_{\text{Cl}}(a_1)]$ and $^3[\text{S}_2^-, \text{V}_{\text{Cl}}(t_2)]$. The nature of these states has been deeply explained previously,^[9] and their orbitals are presented on the density of states of the material (Figure 3). All of these states are located in the bandgap of hackmanite.

Hackmanite shows XEOL and its light yield behaves in a way typical of scintillation, i.e., it increases with increasing X-ray energy. The same applies for the color yield, but it is disturbed by the heating of the material in the synchrotron beam as well as the radiation damage caused by the beam. Nevertheless, we can assume that the coloration is caused by the recombination of the thermalized electron-hole pairs created in a similar electron and hole cascade as in scintillation.

The recombination of the electron and hole generates UV emission (route 1 in Figure 8), which may be partly responsible for the coloring in a similar way as in UV-induced tenebrescence, although its role is probably close to negligible as was shown above. The main coloration mechanism thus involves the migration of a hole and an electron to the $\text{S}_2^{2-}, \text{V}_{\text{Cl}}$ pair. The hole migrates to the π^* state of the $(\text{S}_2)^{2-}$ ion and the electron to the a_1 state of the chloride vacancy (route 2 in Figure 8). Once this electron-hole pair has been created, the system relaxes to create the color center. The color can then be bleached by thermal or optical energy in a similar way as in UV-induced tenebrescence.^[8,9]

2.5. A Possible Application—Tenebrescence Imaging

Based on what has been presented so far, we first tested if hackmanite could be used to indicate X-ray dose by its color intensity in the same way as is possible for UV radiation.^[8] Indeed, a linear dependence between dose and color intensity was observed (Figure 9a) indicating that the material can be used as a visual dosimeter for X-rays. Of course, for practical

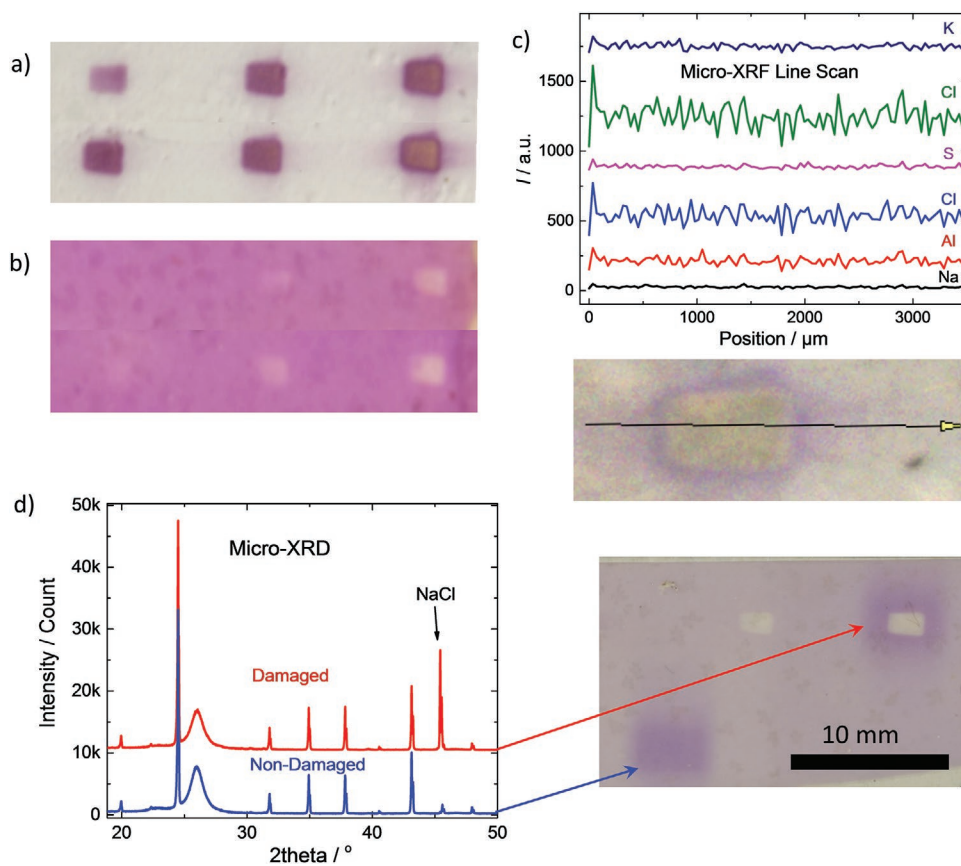


Figure 7. a) Spots of synchrotron X-ray-induced tenebrescence. b) Sample in (a) irradiated with 254 nm UV radiation after bleaching the sample with white light. c) Results of a micro-XRF line scan over a radiation-damaged spot. d) Micro-XRD patterns of a damaged and nondamaged spot as well as a photo of the sample used showing the spots where the diffraction data were collected from.

use, the material must, e.g., be coated with an UV-absorbing layer to prevent coloring induced by a possible presence of UV radiation.

Next, we tested hackmanite's imaging capabilities as a real-world application by using it as an X-ray imaging plate.

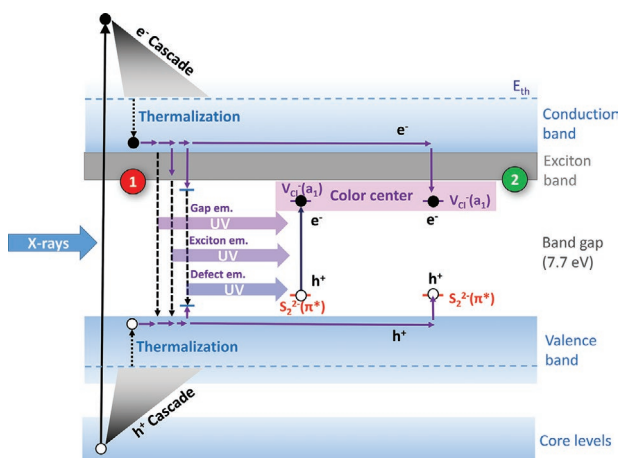


Figure 8. Possible mechanisms of X-ray-induced tenebrescence in hackmanites. More detailed explanation of the color center and its bleaching has been provided earlier.^[8,9]

A deceased ant specimen of unidentified species (Figure 9b) found in nature was used as the sample body to be imaged. The imaging experiment demonstrates how a part where photons were attenuated in the ant's body result in an image where not only the exoskeletal outline, but also details inside the body are visible (Figure 9c,d), and the required equipment except for the X-ray generator is only a simple camera.

This is the first time wherein X-ray imaging using hackmanite's tenebrescence has been reported. Since the dose is relatively high even with only 35 mSv, this type of imaging or dosimetry is most suitable for high-dose X-ray applications used for eliminating undesired organisms or in other cases where the dose received by the irradiated object is irrelevant, e.g. imaging of welds or electronic components for quality control. For example industrial X-ray radiography operates with a typical dose rate of 5–20 Sv h⁻¹^[40] and in the imaging of, e.g., 15 mm steel 10 to 50 s exposure times are commonly used.^[41] This corresponds to doses from 14 to 280 mSv, which is a range well suitable for hackmanites, since they have a photoresponse dose of 180 mSv (corresponding to a photoresponse time of 103 min in the imaging setup used in the present work) (Figure 9e). Furthermore, the coloration contrast at that dose is a good 33%, which extrapolates to a high^[42] 47% of full color intensity (Figure 9f).

The material can thus be exploited to act as a device that measures cumulative doses without the need for proportional

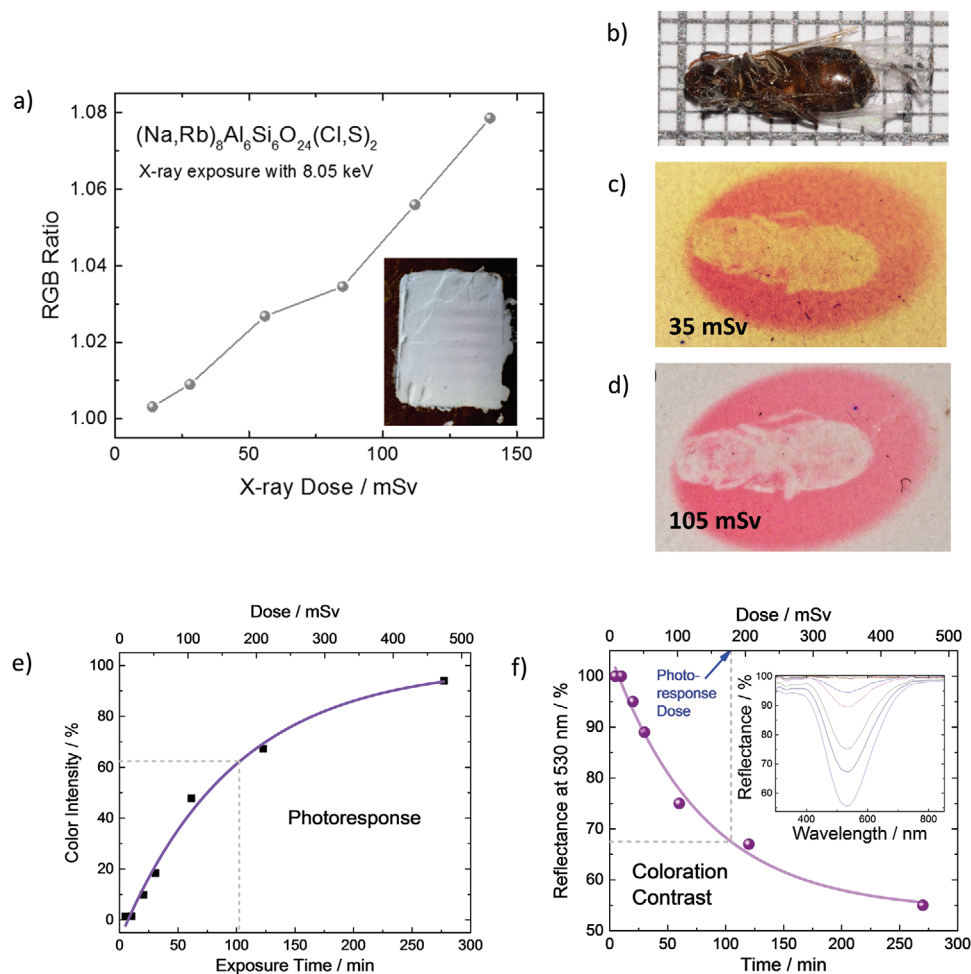


Figure 9. a) Color intensity of the Rb material with different doses of $\text{Cu K}\alpha$ radiation from an X-ray powder diffractometer. b) A deceased ant on a millimeter paper. c) Tenebrescence imaging result of the ant on a tape-cast Na sample (35 mSv dose). d) Same as (c) but with a higher dose (105 mSv). e) Relative color intensity and f) reflectance at 530 nm for the Na sample obtained with different doses and times in the imaging setup used. The inset of (f) shows the respective reflectance spectra. Data in (e) was used to determine the photoresponse time and that in (f) to determine coloration contrast.

counters, scintillators, ionization chambers, semiconductor detectors, imaging systems or other costly equipment requiring skilled operators. Instead, the dose is easily visualized from the color intensity and an image is obtained without a need for any reader systems or conversion to electric signal. This means that hackmanites have great potential for easy on-the-spot use.

3. Conclusion

The present work marks yet another milestone in the understanding of the outstanding properties of smart hackmanite materials. We established the fact that hackmanites' X-ray-induced photochromism proceeds with a mechanism that is very similar to that in scintillation. The marked difference is that scintillation is a very much faster process in both the signal buildup and its disappearance than hackmanites' coloring and decoloring are. Thus, hackmanites cannot be used for fast-reacting live detection or quantification of X-rays. Instead, the slowness of the hackmanites' response gives them

the advantage that they can be used as visual memory devices that conveniently show the accumulated dose as the intensity of color in the material. However, due to the fact that hackmanites contain only light elements, they are not ideally suited for low-dose X-ray applications. Nonetheless, there are many application areas for X-rays, such as sterilization or industrial imaging, which employ higher doses in the range where the hackmanite materials function at their best. Since hackmanite is originally a mineral structure (and thus can be assumed to be stable) and since the coloration involves a very minor structural rearrangement, the material can withstand both high doses and coloration–decoloration cycles practically ad infinitum. This makes the materials highly attractive alternatives in future X-ray dosimetric and photochromic imaging applications.

4. Experimental Section

Sample Preparation: Hackmanite samples were synthesized with a solid-state reaction route described below. The starting materials were

zeolite A (Sigma Aldrich, lot BCBF5787V), NaCl (>99.5%, J. T. Baker), Na₂SO₄ (Merck, >99%), LiCl (99%, Acros), RbCl (≥99.0%, Sigma) and NaBr (J. T. Baker, reagent grade). The samples were prepared by weighing stoichiometric amounts of reagents, i.e., 0.700 g zeolite A (dried at 500 °C for 1 h), 0.240 g NaCl and 0.0600 g Na₂SO₄ when producing Na₈Al₆Si₆O₂₄(Cl,S)₂, 0.700 g zeolite A, 0.496 g RbCl and 0.0600 g Na₂SO₄ when producing (Rb,Na)₈Al₆Si₆O₂₄(Cl,S)₂, 0.700 g zeolite A, 0.0850 g LiCl, 0.1200 g NaCl and 0.0600 g Na₂SO₄ when producing (Li,Na)₈Al₆Si₆O₂₄(Cl,S)₂ and 0.700 g zeolite A, 0.427 g NaBr, and 0.0600 g Na₂SO₄ to produce Na₈Al₆Si₆O₂₄(Br,S)₂. The mixture of powders was ground by hand in an agate mortar and transferred to an alumina crucible and heated at 850 °C in air atmosphere for 48 h and let to cool passively to room temperature. After this, the sample was ground and heated to 850 °C in a flowing N₂/H₂ (88/12%) atmosphere for 2 h and let to cool passively to room temperature. Finally, the sample was ground once again to yield the finished end product. For easy handling, the hackmanite powders were cast as 80 μm thick flexible green tapes with a method modified from that published by Abhinay et al.^[43]

Computational Details: Geometry optimizations were performed with periodic boundary conditions (PBC) within the density functional theory (DFT) framework implemented in the ab initio CRYSTAL17 code.^[44] The global hybrid functional PBE0^[45] was selected along with localized (Gaussian) basis, which is known to give accurate geometrical parameters for sodalites.^[9] All-electron double- ζ basis sets with polarization functions were used for Si, Al, O, Na, and Cl while all-electron triple- ζ basis sets with polarization functions were used for S. The reciprocal space was sampled according to a sublattice with a 12 × 12 × 12 k-points mesh for the geometry optimization of the bulk system while a single k-point (the Γ point) was used for geometry optimization of the 2 × 2 × 2 supercells containing the default sulfur species. The convergence criterion for the self-consistent field (SCF) cycle was fixed at 10⁻⁷ Ha per unit cell. X-ray Absorption Near Edge Spectroscopy calculations were performed using a time-dependent density functional theory formalism implemented in Orca^[44,46,47] with B3LYP/Def2-SVP level of theory. Relativistic corrections were considered thanks to the zero-order regular approximation (ZORA) and RJCOSX approximation was used in order to speed up the calculations. Energy convergence criterion for the SCF cycles was fixed at 10⁻⁸ Ha per unit cell. The excitation window was restricted to the 1s core orbital of the sulfur species of interest, along with the virtual orbitals having an energy higher than the first virtual orbital of the sulfur species, and 240 transitions were computed. These calculations were performed on a cluster extracted from the optimized geometry. This cluster contains the sulfur impurity, the Na₄ tetrahedron and the β -cage surrounding it. Following the previous work,^[48] the cage was surrounded by a shell of cations described by pseudopotentials without the related basis set and a cloud of point charges. Point charges used to simulate the Madelung potential of the crystal were obtained through the Ewald package.^[49] A 5 × 5 × 5 supercell was used to generate the point charges, and the fitting procedure led to an RMS error lower than 1 μV on the Ewald potential.

Characterization: Crystal structure and purity were checked with X-ray powder diffraction measurements using a Huber G670 position sensitive detector and CuK $_{\alpha 1}$ radiation ($\lambda = 1.54060$ Å). Initial UV-coloring test were carried out with hand-held UV lamps UVP UVLS-24 operating with 4 W at 254 or 365 nm as well as UVP UVM-57 operating with 6 W at 302 nm. These lamps give an irradiance of 5.8, 6.4, and 4.3 mW cm⁻², respectively. The irradiances were determined with an Opsytec Dr. Gröbel Radiometer RM 12 equipped with RM12 sensors calibrated for UVA, UVB, and UVC. The initial X-ray coloring tests were done using a PANalytical Epsilon 1 X-ray fluorescence spectrometer equipped with an Ag tube (K $_{\alpha}$ emission at ≈22 keV) as the X-ray source.

The spectral reflectance measurements were conducted with an Avantes AvaSpec ULS2048CL-EVO spectrometer coupled with an Avantes FC-IR600-1-ME-HTX optical fiber. The light source was an Ocean Optics LS-1 Cal calibration lamp directed towards the sample 20 cm away. Color fading curves (spontaneous fading) were measured with the same setup by following the fading of the tenebrescence signal as a function of time. Thermotenebrescence curves were constructed

by following the reflectance (measured with the same setup described above) of an initially fully colored sample as a function of temperature. The heating was carried out using a MikroLab Thermoluminescent Materials Laboratory Reader RA'04 programmed at heating rate of 3 °C s⁻¹. The signal was corrected for spontaneous fading. The tenebrescence bleaching spectra were compiled from reflectance spectra (measured with the same setup described above) collected for a fully colored sample (2 h of X-ray exposure in PANalytical Epsilon 1 XRF machine and 1 min of 254 nm UV irradiation) after an efficient time of exposure (5 min for sample Li, 1 min for sample Br, 1 min for sample Na and 30 s for sample Rb) of selected wavelengths from a 150 Xe lamp. The wavelengths were adjusted using a LOT MSH300 monochromator. The XANES spectra were measured at the Synchrotron Laboratory for Environmental Studies SUL-X beamline at the electron accelerator of the Karlsruhe Institute of Technology in Karlsruhe, Germany. The SUL-X beamline uses a wiggler as radiation source and a Si(111) fixed exit double crystal monochromator for tuning the X-ray energy. The X-ray beam was focused in the case of Li hackmanites with a Kirckpatrick-Baez mirror system to about 150 μm (hor.) and 50 μm (vert.) and was collimated for the Na and Rb and Br hackmanites resulting in beam sizes of about 1.3 mm (hor.) and 0.5 mm (vert.) at sample positions. In one case (track of the pre edge peak maximum) a focused beam of about 50 μm (hor.) and 50 μm (vert.) was used. Energy was calibrated to 2481.4 eV at the maximum of the sulfate peak of the S K-edge XANES spectrum of a Scotch tape. S K α fluorescence emission intensities were measured with a seven element silicon drift diode detector with 12.5 μm DuraBeryllium windows (type SiriusSD-M7 × 65133-BE-INC-V, Rayspec) at xmap and falcon electronics (XIA). S K α fluorescence emission was used to record the intensities of the pre-edge maximum during irradiation, the complete pre-edge peak and S K XANES spectra. Energy step widths across the pre-edge and absorption edge were 0.2 eV. All measurements were carried out under vacuum.

The synchrotron X-ray irradiations and related measurements were conducted at the Synchrotron Laboratory for Environmental Studies SUL-X beamline at the Karlsruhe Institute of Technology in Karlsruhe, Germany. For the XEOL measurements, an Avantes AvaSpec ULS2048CL-EVO spectrometer coupled with an Avantes FC-IR600-1-ME-HTX optical fiber was used in scope mode. The tenebrescence rise curves and the reflectance spectra were measured with the same spectrometer (in reflectance mode) and fiber using an Ocean Optics LS-1 Cal calibration lamp directed towards the sample 20 cm away. Vacuum ultraviolet (VUV) spectroscopy measurements were performed at the Toroidal Grating Monochromator (TGM)^[50] beamline from the Brazilian Synchrotron Light Laboratory (LNLS), with quartz filters to avoid higher harmonic excitation. The emission spectra were registered with an optical fiber coupled to an Ocean Optics QE65000 spectrometer. Cathodochromism, i.e., electron beam induced coloring, was induced with a setup consisting of a Nuclide Corporation ELM2EX Luminoscope equipped with a Nuclide Corporation ELM2B vacuum chamber. The color intensity was determined outside the vacuum chamber (i.e., ex situ) from reflectance spectra measured using the same setup described above.

The micro-XRF line scan was collected using a Bruker Tornado M4 micro-XRF spectrometer. Micro-XRD measurements were carried out using a PANalytical Empyrean diffractometer with CuK $_{\alpha 1,2}$ radiation. The setup yielded a 0.4 mm × 0.5 mm irradiation area on the sample surface. Tests for X-ray dose-dependent color intensity were carried out using a Panalytical X'Pert Pro MPD X-ray diffractometer with CuK $_{\alpha 1,2}$ radiation. The doses were measured with a Thermo Scientific RadEye B20-ER device. Then the sample was photographed and the RGB values for the irradiated and nonirradiated parts were determined using the ImageJ program.^[51] The nonirradiated:irradiated RGB ratio was then used as the color intensity at each dose. The tenebrescence imaging experiments were done using the PANalytical Epsilon 1 X-ray fluorescence spectrometer equipped with an Ag tube (K $_{\alpha}$ emission at ≈22 keV) as the X-ray source. The doses were measured with the Thermo Scientific RadEye B20-ER. The photoresponse time (≈63% of full coloration^[42]) was determined from the reflectance spectra (measured

with an Avantes AvaSpec HS-TEC spectrometer coupled with an Avantes FC-IR600-1-ME-HTX optical fiber. The light source was a 60-W incandescent lamp producing continuous spectrum, directed towards the sample 50 cm away) of the Na sample in a series that received 5, 10, 20, 30, 60, 120, and 270 min (8.7, 17.5, 35.0, 52.5, 105, 210, and 474 mSv, respectively) of X-ray exposure from the PANalytical Epsilon 1 X-ray fluorescence spectrometer. The results were fitted to converge with an asymptotic function in OriginPro 2016 64-bit b9.3.2.303.^[52] The 100% photochromic change value is calculated from this fit, and this value was used as the maximum photochromic change reference in the calculations.^[42] Coloration contrast values^[42] were obtained from the difference in reflectance at 530 nm between a nonexposed sample and the sample exposed to a known dose.

Supporting Information

Supporting Information is available from the Wiley Online Library or from the author.

Acknowledgements

Business Finland is gratefully acknowledged for financial support (project #2291/31/2017). The authors thank the SYSPROD project and AXELERA Pôle de Compétitivité for financial support (PSMN Data Center). This work was granted access to the HPC resources of CINES, IDRIS, and TGCC under the allocation 2018–080609 made by GENCI. The authors acknowledge the French agency ANR (TeneMod project ANR-17-CE29-0007-21) for financial support. The authors gratefully acknowledge the support of the Centre Blaise Pascal's IT test platform at ENS de Lyon (Lyon, France) for its facilities. The platform operates the SIDUS solution developed by Emmanuel Quemener. FAPESP—São Paulo Research Foundation, Brazil (project #2018/05280-5) and CNPEM for providing the beamtime at the TGM beamline of LNLS (#20180001) are acknowledged. H.P. and P.P. acknowledge Jenny and Antti Wihuri Foundation for financial support. Dr. Thomas Spangenberg is thanked for his tireless help at KIT.

Conflict of Interest

The authors declare no conflict of interest.

Data Availability Statement

The data that support the findings of this study are available from the corresponding author upon reasonable request.

Keywords

dosimetry, imaging, photochromism, sodalite, X-ray detection

Received: April 14, 2021

Revised: June 4, 2021

Published online:

- [1] J. W. Anthony, R. A. Bideaux, K. W. Bladh, M. C. Nichols, *Handbook of Mineralogy*, Mineralogical Society Of America, Chantilly, VA **2001**.
[2] W. A. Deer, R. A. Howie, W. S. Wise, J. Zussman, *Rock-Forming Minerals – Framework Silicates*, The Geological Society, London **2004**.

- [3] I. Norrbo, P. Gluchowski, I. Hyppänen, T. Laihininen, P. Laukkanen, J. Mäkelä, F. Mamedov, H. S. Santos, J. Sinkkonen, M. Tuomisto, A. Viinikanoja, M. Lastusaari, *ACS Appl. Mater. Interfaces* **2016**, *8*, 11592.
[4] E. R. Williams, A. Simmonds, J. A. Armstrong, M. T. Weller, *J. Mater. Chem.* **2010**, *20*, 10883.
[5] I. Norrbo, J. M. Carvalho, P. Laukkanen, J. Mäkelä, F. Mamedov, M. Peurla, H. Helminen, S. Pihlasalo, H. Härmä, J. Sinkkonen, M. Lastusaari, *Adv. Funct. Mater.* **2017**, *27*, 1606547.
[6] D. B. Medved, *Am. Mineral.* **1954**, *39*, 615.
[7] I. Norrbo, P. Gluchowski, P. Paturi, J. Sinkkonen, M. Lastusaari, *Inorg. Chem.* **2015**, *54*, 7717.
[8] I. Norrbo, A. Curutchet, A. Kuusisto, J. Mäkelä, P. Laukkanen, P. Paturi, T. Laihininen, J. Sinkkonen, E. Wetterskog, F. Mamedov, T. Le Bahers, M. Lastusaari, *Mater. Horiz.* **2018**, *5*, 569.
[9] A. Curutchet, T. Le Bahers, *Inorg. Chem.* **2017**, *56*, 414.
[10] J. A. Armstrong, M. T. Weller, *Chem. Commun.* **2006**, 1094.
[11] M.-S. Wang, C. Yang, G.-E. Wang, G. Xu, X.-Y. Lv, Z.-N. Xu, R.-G. Lin, L.-Z. Cai, G.-C. Guo, *Angew. Chem., Int. Ed. Engl.* **2012**, *51*, 3432.
[12] H. Zhang, X. Wu, *Adv. Sci.* **2016**, *3*, 1500224.
[13] C. Chen, J.-K. Sun, Y.-J. Zhang, X.-D. Yang, J. Zhang, *Angew. Chem., Int. Ed. Engl.* **2017**, *56*, 14458.
[14] A.-P. Jin, Z.-W. Chen, M.-S. Wang, G.-C. Guo, *Dyes Pigm.* **2019**, *163*, 656.
[15] S.-L. Li, M. Han, Y. Zhang, G.-P. Li, M. Li, G. He, X.-M. Zhang, *J. Am. Chem. Soc.* **2019**, *141*, 12663.
[16] C. Doelter, *Handbuch der Mineralchemie*, Verlag von Theodor Steinkopff, Dresden, Germany **1912**.
[17] O. Stuhlman, A. F. Daniel, *J. Opt. Soc. Am.* **1928**, *17*, 289.
[18] F. H. Pough, T. H. Rogers, *Am. Mineral.* **1947**, *32*, 31.
[19] E. W. Claffy, *Am. Mineral.* **1953**, *38*, 919.
[20] R. D. Kirk, *Am. Mineral.* **1955**, *40*, 276.
[21] R. D. Kirk, *J. Electrochem. Soc.* **1954**, *101*, 461.
[22] R. Chen, V. Pagonis, *Thermally and Optically Stimulated Luminescence: A Simulation Approach*, Wiley, Wiltshire, UK **2011**.
[23] J. Goettlicher, A. Kotelnikov, N. Suk, A. Kovalski, T. Vitova, R. Steininger, *Z. Kristallogr.* **2013**, *228*, 157.
[24] M. Fleet, X. Liu, S. Harmer-Bassell, P. King, *Can. Mineral.* **1605**, *43*, 1605.
[25] J. G. A. Rogalev, in *Chemical Applications of Synchrotron Radiation*, (Ed: T.-K. Sham), World Scientific, Singapore **2002**, p. 736.
[26] D. S. McGregor, *Annu. Rev. Mater. Res.* **2018**, *48*, 245.
[27] C. Agamah, S. Vuori, P. Colinet, I. Norrbo, J. M. de Carvalho, L. K. Okada Nakamura, J. Lindblom, L. van Goethem, A. Emmermann, T. Saarinen, T. Laihininen, E. Laakkonen, J. Lindén, J. Konu, H. Vrielinck, D. Van der Heggen, P. F. Smet, T. Le Bahers, M. Lastusaari, *Chem. Mater.* **2020**, *32*, 8895.
[28] A. Thompson, D. Attwood, E. Gullikson, M. Howels, K.-J. Kim, J. Kirz, J. Kortright, I. Linday, Y. Liu, P. Pianetta, A. Robinson, J. Scofield, J. Underwood, G. Williams, H. Winick, *X-ray data booklet*, <https://xdb.lbl.gov/xdb-new.pdf> (accessed: November 2020).
[29] W. Phillips, *J. Electrochem. Soc.* **1970**, *117*, 1557.
[30] C. Z. van Doorn, D. J. Schipper, P. T. Bolwijn, *J. Electrochem. Soc.* **1972**, *119*, 85.
[31] M. J. Berger, J. H. Hubbell, S. M. Seltzer, J. Chang, J. S. Coursey, R. Sukumar, D. S. Zucker, K. Olsen, NIST XCOM, <https://physics.nist.gov/PhysRefData/Xcom/html/xcom1.html> (accessed: November 2020).
[32] A. J. Warren, D. Axford, R. L. Owen, *J. Synchrotron Radiat.* **2019**, *26*, 991.
[33] A. Kastengren, *J. Synchrotron Radiat.* **2019**, *26*, 205.
[34] H. Wallander, J. Wallentin, *J. Synchrotron Radiat.* **2017**, *24*, 925.
[35] J. Lahtinen, H. Arvela, R. Pöllänen, M. Moring, in *Radiation in the Environment (Säteily Ympäristössä)*, Karisto, Hämeenlinna, Finland **2003**, pp. 302–341.
[36] P. J. R. Montes, M. E. G. Valerio, G. de, M. Azevedo, *Nucl. Instrum. Methods Phys. Res., Sect. B* **2008**, *266*, 2923.

- [37] M. V. D. S. Rezende, A. B. Andrade, M. E. G. Valerio, P. J. R. Montes, *J. Appl. Phys.* **2014**, *115*, 103510.
- [38] International Centre for Diffraction Data. PDF-4+. Entry 00-005-0628 (NaCl) **2020**.
- [39] M. Oliva-Ramirez, M. Macías-Montero, A. Borrás, A. R. González-Elipse, *RSC Adv.* **2016**, *6*, 3778.
- [40] M. Kaituri, S. Väisälä, H. Korpela, *Use of Radiation in Industry and in Research (Säteilyn Käyttö Teollisuudessa ja Tutkimuksessa)*, Karisto, Hämeenlinna, Finland **2004**.
- [41] *Industrial Radiography: Image Forming Techniques*, GE Inspection Technologies, Pennsylvania, USA **2008**.
- [42] Z. Yang, J. Du, L. I. D. J. Martin, D. Van der Heggen, D. Poelman, *Laser Photonics Rev.* **2021**, *15*, 2000525.
- [43] S. Abhinay, R. Mazumder, A. Seal, A. Sen, *J. Eur. Ceram. Soc.* **2016**, *36*, 3125.
- [44] R. Dovesi, A. Erba, S. Salustro, B. Kirtman, R. O. C. M. Zicovich-Wilson, B. Civalleri, L. Maschio, M. Rérat, S. Casassa, J. Baima, *WIREs Comput. Mol. Sci.* **2018**, *8*, e1360.
- [45] C. Adamo, V. Barone, *J. Chem. Phys.* **1999**, *110*, 6158.
- [46] F. Neese, *WIREs Comput. Mol. Sci.* **2012**, *2*, 73.
- [47] F. Neese, *WIREs Comput. Mol. Sci.* **2017**, *8*, e1327.
- [48] P. Colinet, A. Gheeraert, A. Curutchet, T. Le Bahers, *J. Phys. Chem. C* **2020**, *124*, 8949.
- [49] M. Klintonberg, S. E. Derenzo, M. J. Weber, *Comput. Phys. Commun.* **2000**, *131*, 120.
- [50] R. L. Cavasso Filho, A. F. Lago, M. G. P. Homem, S. Pilling, A. Naves de Brito, *J. Electron Spectrosc. Relat. Phenom.* **2007**, *156–158*, 168.
- [51] C. A. Schneider, W. S. Rasband, K. W. Eliceiri, *Nat. Methods* **2012**, *9*, 671.
- [52] *Origin 2016*, OriginLab Corporation, USA **2016**.